Dalton Transactions

PAPER

View Article Online
View Journal | View Issue

Cite this: *Dalton Trans.*, 2016, **45**, 12559

The contrasting effect of the Ta/Nb ratio in (111)-layered B-site deficient hexagonal perovskite $Ba_5Nb_{4-x}Ta_xO_{15}$ crystals on visible-light-induced photocatalytic water oxidation activity of their oxynitride derivatives†

Mirabbos Hojamberdiev,[a] Maged F. Bekheet,[b] Ehsan Zahedi,[c] Hajime Wagata,[a] Junie Jhon M. Vequizo,[d] Akira Yamakata,[d] Kunio Yubuta,[e] Aleksander Gurlo,[b] Kazunari Domen[f] and Katsuya Teshima*[a,g]

Received 25th May 2016,
Accepted 4th July 2016

DOI: 10.1039/c6dt02095j

www.rsc.org/dalton

The effect of the Ta/Nb ratio in the (111)-layered B-site deficient hexagonal perovskite $Ba_5Nb_{4-x}Ta_xO_{15}$ ($0 \le x \le 4$) crystals grown by a KCl flux method on visible-light-induced photocatalytic water oxidation activity of their oxynitride derivatives $BaNb_{1-x}Ta_xO_2N$ ($0 \le x \le 1$) was investigated. The Rietveld refinement of X-ray data revealed that all $Ba_5Nb_{4-x}Ta_xO_{15}$ samples were well crystallized in the space group $P\bar{3}m1$ (no. 164). Phase-pure $BaNb_{1-x}Ta_xO_2N$ ($0 \le x \le 1$) porous structures were obtained by nitridation of the flux-grown oxide crystals at 950 °C for 20, 25, 30, 35, and 40 h, respectively. The absorption edge of $BaNb_{1-x}Ta_xO_2N$ ($0 \le x \le 1$) was slightly shifted from 720 to 690 nm with the increasing Ta/Nb ratio. The O_2 evolution rate gradually progressed and reached the highest value (127.24 μmol in the first 2 h) with the Ta content up to 50 mol% but decreased at 75 and 100 mol% presumably due to the reduced specific surface area and high density of structural defects, such as grain boundaries acting as recombination centers, originated from high-temperature nitridation for prolonged periods. Transient absorption spectroscopy provided evidence for the effect of the Ta/Nb ratio on the behavior and energy states of photogenerated charge carriers, indicating a direct correlation with photocatalytic water oxidation activity of $BaNb_{1-x}Ta_xO_2N$.

1. Introduction

As an artificial photosynthesis process, photocatalytic water splitting, in which molecular hydrogen and oxygen are directly dissociated from water molecules using semiconductor photocatalysts and solar energy, has been regarded as one of the most economical processes to produce clean and renewable hydrogen energy on a large scale.[1–5] Layered compounds ($AB_2Nb_3O_{10}$ and $ALaNb_2O_7$ (A = H, K, Rb, Cs; B = Ca, Sr)) consist of negatively charged perovskite layers and A^+ cations in the interlayer gallery have also been demonstrated to be semiconductor photocatalysts for water splitting.[6] As is known, electrons and holes are generated in sheets upon light irradiation, commencing the redox reactions with reactant molecules adjacent to the layers. Maeda and Mallouk[7] examined three different restacked perovskite nanosheets ($HCa_2Nb_3O_{10}$, $HSr_2Nb_3O_{10}$ and $LaNb_2O_7$) as photocatalysts for H_2 evolution from water containing 2-propanol under UV light irradiation and found that the tilting of NbO_6 octahedra in the perovskite layers affects the overall photocatalytic activity.

[a]*Department of Environmental Science and Technology, Faculty of Engineering, Shinshu University, 4-17-1 Wakasato, Nagano 380-8553, Japan. E-mail: teshima@shinshu-u.ac.jp; Fax: +81-26-269-5550; Tel: +81-26-269-5556*
[b]*Fachgebiet Keramische Werkstoffe, Institut für Werkstoffwissenschaften und -technologien, Technische Universität Berlin, Hardenbergstraße 40, 10623 Berlin, Germany*
[c]*Department of Physical Chemistry, Shahrood Branch, Islamic Azad University, Shahrood, Iran*
[d]*Graduate School of Engineering, Toyota Technological Institute, 2-12-1 Hisakata, Tempaku, Nagoya 468-8511, Japan*
[e]*Institute for Materials Research, Tohoku University, 2-1-1 Katahira, Aoba-ku, Sendai 980-8577, Japan*
[f]*Department of Chemical System Engineering, School of Engineering, The University of Tokyo, 7-3-1 Hongo, Bunkyo-ku, Tokyo 113-8656, Japan*
[g]*Center for Energy and Environmental Science, Shinshu University, 4-17-1 Wakasato, Nagano 380-8553, Japan*

†Electronic supplementary information (ESI) available: Selected interatomic distances and bonding angles from crystal structure refinement for $Ba_5Nb_{4-x}Ta_xO_{15}$ at 293 K. The EDS element mapping images and spectra and IR absorption spectra of $BaNb_{1-x}Ta_xO_2N$ ($0 \le x \le 1$) crystal structures. CCDC 1473461–1473463, 1473465 and 1473466. For ESI and crystallographic data in CIF or other electronic format see DOI: 10.1039/c6dt02095j

Among layered oxides, (111)-layered perovskites $A_5M_4O_{15}$ (A = Sr, Ba; M = Ta, Nb) have also exhibited high photocatalytic activity for water splitting under UV light.[8–11] Monomolecular-layer perovskite $Ba_5Ta_4O_{15}$ and $Ba_5Nb_4O_{15}$ nanosheets with hexagonal structures synthesized by a hydrothermal method exhibited high photocatalytic activity in the photodegradation of Rhodamine B and gaseous formaldehyde as well as in the evolution of H_2 from water splitting under UV light irradiation, respectively.[12,13] Marschall and co-workers[14] have pointed out that the combination of effective charge carrier separation and improved electron transfer in highly crystalline multi-component heterojunction photocatalysts consisting of $Ba_5Ta_4O_{15}$, $Ba_3Ta_5O_{15}$ and $BaTa_2O_6$ modified with Rh–Cr_2O_3 core–shell co-catalyst systems can induce an enhanced photocatalytic activity for overall water splitting under UV light irradiation. Also, the $Ba_5Ta_4O_{15}$/$Ba_3Ta_5O_{15}$ photocatalyst composite showed superior hydrogen evolution up to 1885 μmol h^{-1} with only 0.025 wt% Rh due to the improved charge carrier separation.[15] $Ba_5Ta_4O_{15}$ loaded with Cr_2O_3 nanoparticles also showed an enhanced photocatalytic activity for overall water splitting owing to a dual function of Cr_2O_3: (i) suppressing the back reaction on Rh and (ii) acting as an oxygen evolution reaction co-catalyst.[16] Rh–Cr_2O_3-deposited $Ba_5Ta_4O_{15}$, $Ba_5Ta_2Nb_2O_{15}$ and $Ba_5Nb_4O_{15}$ nanofibers fabricated by electrospinning exhibited better activity in overall water splitting compared to sol–gel-derived powders.[17] Mukherji *et al.*[18] achieved ~50% increment in photocatalytic hydrogen production from water using nitrogen-doped $Ba_5Ta_4O_{15}$ under simulated solar irradiation.

Although $Ba_5Ta_4O_{15}$ and $Ba_5Nb_4O_{15}$ in bulk as well as in nanosheet forms have been separately investigated as photocatalysts for hydrogen generation from water splitting and photodegradation of organic pollutants, the effect of the Ta/Nb ratio in (111)-layered $Ba_5Nb_{4-x}Ta_xO_{15}$ crystals on photocatalytic activity of their oxynitride derivatives has not been reported yet. In this contribution, we particularly demonstrate a contrasting effect of the Ta/Nb ratio in (111)-layered B-site deficient hexagonal perovskite $Ba_5Nb_{4-x}Ta_xO_{15}$ crystals grown by a KCl flux method on visible-light-induced photocatalytic water oxidation activity of their oxynitride derivatives ($BaNb_{1-x}Ta_xO_2N$). On the basis of the results obtained from transient absorption spectroscopy (TAS), we also provide evidence for the effect of the Ta/Nb ratio on the behavior and energy states of photogenerated charge carriers (*e.g.*, free electrons, trapped electrons, and holes) to correlate with photocatalytic water oxidation activity of $BaNb_{1-x}Ta_xO_2N$.

2. Experimental

2.1. Crystal growth and nitridation

$Ba_5Nb_{4-x}Ta_xO_{15}$ (x = 0, 1, 2, 3 and 4) crystals were grown by a flux method using a KCl flux. All reagents used in this study were purchased from Wako Pure Chemical Industries, Ltd. Reagent-grade $BaCO_3$, Nb_2O_5, Ta_2O_5, and KCl (>99%) were dry mixed manually in stoichiometric ratios for 30 min using an agate mortar and a pestle. The well-homogenized mixture (10 g) with 10 mol% solute concentration was placed in a platinum crucible with a capacity of 30 cm^3 and closed loosely with a platinum lid, heated at 1000 °C for 10 h at a heating rate of 50 °C h^{-1} and cooled at a cooling rate of 150 °C h^{-1}. The resulted crystals were separated from the remaining flux by washing with warm water repeatedly and dried at 100 °C for 12 h. The oxynitride derivatives, $BaNb_{1-x}Ta_xO_2N$ ($0 \le x \le 1$), were synthesized by nitridation of the flux-grown oxide crystals at 950 °C for 20, 25, 30, 35 and 40 h under an NH_3 flow (200 mL min^{-1}), followed by acid treatment (dilute HNO_3), rinsing with water and drying.

2.2. Characterization

The X-ray powder diffraction data were collected in a flat-sample transmission geometry on a STOE STADI P X-ray diffractometer with Mo Kα1 radiation (λ = 0.709260 Å) and a position sensitive detector with a 6° aperture. Rietveld refinement was performed using the FULLPROF program,[19] and profile function 7 (Thompson-Cox-Hastings pseudo-Voigt convoluted with axial divergence asymmetry function)[20] was used in all refinements. The resolution function of the instrument was obtained from the structure refinement of silicon standard (Sigma-Aldrich, ~325 mesh, 99% trace metals basis). The refined parameters included the scale factor, zero-point of detector, background parameters, lattice parameters, atomic occupation factors of Nb/Ta, atomic position coordinates, isotropic atomic displacement parameters (B_{iso}) and asymmetric parameters. The X-ray diffraction (XRD) patterns of oxynitride samples were acquired with a MiniflexII (Rigaku) diffractometer under Cu Kα radiation (λ = 0.15418 nm) in the 2θ scan range of 20° to 70° and compared with entries from the ICDD-PDF-2 powder pattern database. The scanning electron microscopy (SEM) images were taken with a JSM-7600F field-emission-type scanning electron microscope (JEOL), at an acceleration voltage of 15 kV, interfaced with energy-dispersive X-ray spectroscopy (EDS). The ultraviolet-visible (UV-Vis) diffuse reflectance spectra were recorded on a JASCO V-670 spectrophotometer equipped with an integrating sphere, and $BaSO_4$ was used as a reference. The Brunauer–Emmett–Teller (BET) specific surface area was determined from the N_2 adsorption–desorption isotherm measured with a BELSORP-mini instrument (BEL Japan, Inc.) at 77 K after degassing the sample at 120 °C for 12 h. The surface chemical compositions of oxynitride samples were analyzed by X-ray photoelectron spectroscopy (JPS-9010MC, JEOL) under non-monochromatic Mg Kα radiation (1253.6 eV). The XPS profiles were fitted using a Gaussian–Lorentzian function, and the peak positions were normalized by positioning the C 1s peak at 284.5 eV. The concentration of major cations in oxide and oxynitride samples was analyzed by inductively coupled plasma optical emission spectrometry (SPS5510, SII Nanotechnology Inc.). The effect of the Ta/Nb ratio on the behavior and energy states of photogenerated charge carriers (*e.g.*, free electrons, trapped electrons, and holes) in $BaNb_{1-x}Ta_xO_2N$ was further studied by transient absorption spectroscopy (TAS).[21–25]

2.3. Photocatalytic water oxidation test

The photocatalytic water oxidation half-reactions were performed in a side-irradiation-type reactor connected to a closed gas circulation system, equipped with a gas chromatograph (GC-8A, TCD, Ar gas carrier, Shimadzu) and a vacuum pump, under visible light irradiation (300 W Xe lamp with a cutoff filter (λ > 420 nm)) using 100 mg of $BaNb_{1-x}Ta_xO_2N$ (x = 0, 0.25, 0.50, 0.75, and 1.0) loaded with CoO_x (2 wt% Co) nanoparticles as an O_2 evolution cocatalyst. 200 mg of La_2O_3 and 300 mL of 10 mM $AgNO_3$ aqueous solution were employed as a pH buffer and a sacrificial electron scavenger, respectively. Before irradiation, the reactor was purged with Ar (20 mL min^{-1}) for 2 h to eliminate oxygen. CoO_x nanoparticles were loaded by immersing the oxynitride samples in aqueous solution of $Co(NO_3)_2{\cdot}6H_2O$ (>99.5%, Wako Pure Chemical Industries, Ltd), followed by heating at 700 °C for 1 h under an NH_3 flow (200 mL min^{-1}) and reoxidizing at 200 °C for 1 h in air.

3. Results and discussion

The XRD patterns of $Ba_5Nb_{4-x}Ta_xO_{15}$ (x = 0, 1, 2, 3 and 4) are shown in Fig. 1. All samples were well crystallized with a trigonal crystal system (space group $P\bar{3}m1$, no. 164), corresponding to the B-cation deficient perovskite structure of $Ba_5M_4O_{15}$ (M = Nb and Ta).[26,27] No characteristic peaks belonging to impurity phases were observed in all samples. The crystal structures of $Ba_5Nb_4O_{15}$ [26] and $Ba_5Ta_4O_{15}$ [27] were used as initial models for x = 0 and 4, respectively. For x = 1, 2 and 3, the refined structural model obtained for the $Ba_5Nb_4O_{15}$ phase was used as the initial model, and the occupancy of the Nb^{5+} and Ta^{5+} cations on the two crystallographic sites B1 and B2 (Table 1) for B-site atoms was refined and subjected to the total site occupancy being unity and the constraint of the chemical composition. For all samples, isotropic atomic displacement parameters (B_{iso}) were constrained to be equal for all oxygen atoms despite

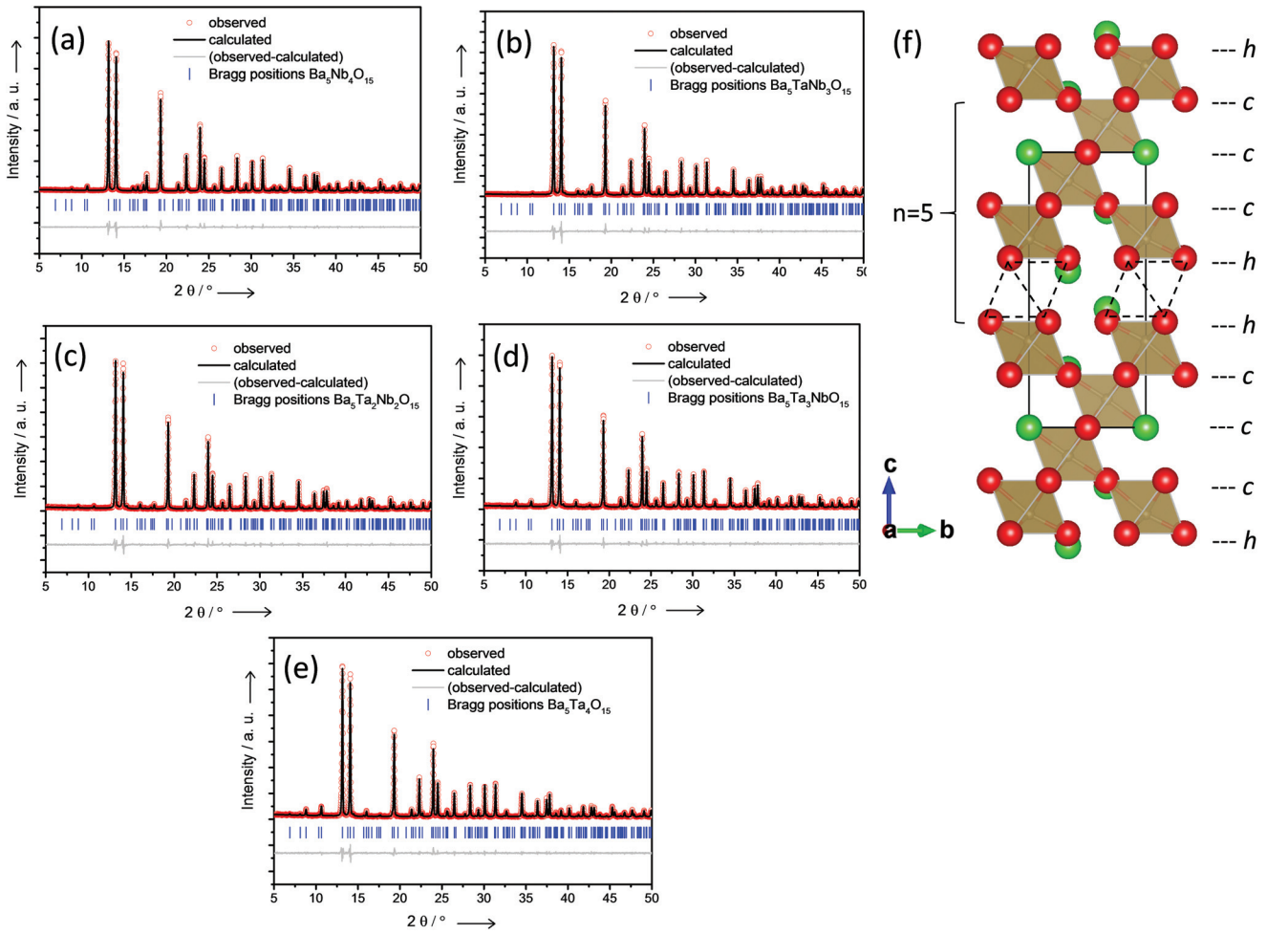

Fig. 1 Structure refinement of X-ray powder diffraction data of (a) $Ba_5Nb_4O_{15}$, (b) $Ba_5Nb_3TaO_{15}$, (c) $Ba_5Nb_2Ta_2O_{15}$, (d) $Ba_5NbTa_3O_{15}$ and (e) $Ba_5Ta_4O_{15}$, indicating the observed (red circle) and calculated (black line) intensities, the calculated Bragg reflections (blue tick) and the difference (gray line). (f) (100) projection of the crystal structure of $Ba_5Nb_{4-x}Ta_xO_{15}$, showing Ba ions (light green spheres), oxygen anions (red spheres), Nb/Ta ions occupying the $(Nb/Ta)O_6$ octahedra (olive), and empty octahedra (dashed line). $Ba_5Nb_{4-x}Ta_xO_{15}$ are the n = 5 member of the B-cation deficient perovskite-like $A_nB_{n-1}O_{3n}$ series, in which the n – 1 layers of BO_6 octahedra are extended along the (111) planes. The packing sequence of this perovskite structure is *ccchh*. The results of the ICP-OES analysis indicate that the Ta/Nb ratio gradually increases, and the chemical compositions of $Ba_5Nb_{4-x}Ta_xO_{15}$ crystals are close to their stoichiometric starting mixtures (Table 2).

Table 1 Structural parameters from crystal structure refinement for $Ba_5Nb_{4-x}Ta_xO_{15}$ at 293 K in the space group $P\bar{3}m1$ (no. 164); $Z = 1$

Atoms/positions	Parameters	$x = 0$	$x = 1$	$x = 2$	$x = 3$	$x = 4$
Ba1	B_{iso} (Å^2)[b]	0.21(9)	0.57(13)	0.30(16)	0.67(5)	0.41(12)
1a (0,0,0)[a]						
Ba2	z	0.7914(2)	0.7911(3)	0.7896(4)	0.7896(3)	0.7872(3)
2d (1/3,2/3,z)	B_{iso} (Å^2)	0.52(6)	0.48(8)	0.66(11)	0.67(5)	0.26(10)
Ba3	z	0.4272(2)	0.4264(3)	0.4274(4)	0.4292(4)	0.4304(3)
2d (1/3,2/3,z)	B_{iso} (Å^2)	0.58(5)	0.67(7)	0.70(9)	0.67(5)	1.03(11)
(Nb/Ta)1	z	0.6813(3)	0.6804(4)	0.6830(4)	0.6847(3)	0.6859(2)
2c (0,0,z)	B_{iso} (Å^2)	0.26(4)	0.27(12)	0.20(13)	0.53(9)	0.22(6)
	occ. (Nb/Ta)[c]	1/0	0.858(9)/0.142(9)	0.627(12)/0.373(12)	0.318(12)/0.682(12)	0/1
(Nb/Ta)2	z	0.1041(4)	0.1035(4)	0.1031(4)	0.1033(3)	0.1029(3)
2d (1/3,2/3,z)	B_{iso} (Å^2)	0.26(4)	0.24(7)	0.28(9)	0.12(7)	0.20(8)
	occ. (Nb/Ta)	1/0	0.642(9)/0.358(9)	0.373(12)/0.627(12)	0.182(12)/0.818(12)	0/1
O1	B_{iso} (Å^2)	0.21(8)	0.42(11)	0.48(14)	0.66(15)	0.21(16)
3e (1/2,0,0)						
O2	x	0.171(1)	0.167(2)	0.166(3)	0.166(2)	0.168(2)
6i (x,y,z)	y	−0.171(1)	−0.167(2)	−0.166(3)	−0.166(2)	−0.168(2)
	z	0.1935(11)	0.1924(15)	0.1924(17)	0.1913(16)	0.1922(17)
	B_{iso} (Å^2)	0.21(8)	0.42(11)	0.48(14)	0.66(15)	0.21(16)
O3	x	0.163(1)	0.163(2)	0.162(2)	0.1614(19)	0.164(2)
6i (x,y,z)	y	−0.163(1)	−0.163(2)	−0.162(2)	−0.1614(19)	−0.164(2)
	z	0.6142(12)	0.6148(15)	0.6163(18)	0.6164(16)	0.6159(16)
	B_{iso} (Å^2)	0.21(8)	0.42(11)	0.48(14)	0.66(15)	0.21(16)
Lattice parameters	a (Å^2)	5.7946(1)	5.7958(1)	5.7947(2)	5.79455(6)	5.7892(1)
	c (Å^2)	11.7876(2)	11.7965(2)	11.8030(2)	11.8158(1)	11.8202(2)
Cell volume	V (Å^3)	342.77(1)	343.16(1)	343.24(1)	343.58(1)	343.08(1)
Reliability factors (%)	R_p	6.9	7.3	6.7	6.8	6.1
	R_{wp}	9.6	9.8	9.1	9.0	8.0
	R_{exp}	6.4	7.0	7.0	7.8	6.7
	R_{Bragg}	2.2	2.3	2.3	2.0	2.2
	X^2	2.2	1.9	1.7	1.3	1.4

[a] Wyckoff positions (fractional atomic coordinates). [b] Isotropic temperature factors. [c] Occupation factor.

their occupation at different crystallographic sites to prevent them from tending to small negative values when refined independently. Fig. 1a–e show the observed, calculated and the difference profile for the final cycle of the structure refinement. The final structure parameters of $Ba_5Nb_{4-x}Ta_xO_{15}$, Bragg factor R_B, crystallographic factor R_F and other Rietveld R-factors are given in Table 1. As shown in Fig. 1f, the crystal structure of $Ba_5Nb_{4-x}Ta_xO_{15}$ belongs to the B-cation deficient hexagonal perovskite-like $A_nB_{n-1}O_{3n}$, in which the $n - 1$ layers of BO_6 octahedra are extended along the (111) planes.[26,28] This $Ba_5Nb_{4-x}Ta_xO_{15}$ structure can be described as three cubic close packing (ccp) layers of corner-shared distorted NbO_6 and/or TaO_6 octahedra with a vacant layer in the middle of two hexagonal close packing (hcp) layers of face-shared NbO_6 and/or TaO_6 octahedra, with the (ccchh)-type sequence. The NbO_6 and/or TaO_6 octahedra are separated by cuboctahedron BaO_{12} with large Ba^{2+} ions as interlayer counterions. The vacant octahedral layers are important to minimize the electrostatic repulsion between the highly charged Nb^{5+} and Ta^{5+} ions and stabilize the crystal structure. Since Nb^{5+}/Ta^{5+} cations are located in two different crystallographic sites, B1 and B2 at Wyckoff positions 2c and 2d, respectively (Table 1), two different distortions of BO_6 are expected. The $(B2)O_6$ octahedra, which are in the centers of the perovskite slabs, have two sets of quite similar Nb/Ta–O distances, whereas the $(B1)O_6$ octahedra, which are close to the vacant layers, have two quite different sets of Nb/Ta–O distances, indicating much larger distortion from the centrosymmetric environment at the B1 site. The bond lengths in $Ba_5Nb_{4-x}Ta_xO_{15}$ resulted from the Rietveld refinement are listed in Table S1 in the ESI.† The refinement of the B-cation site distribution in $x = 1$, 2 and 3 shows that the Ta^{5+} cations prefer the B2 sites in the centers of the perovskite blocks over the B1 sites which are close to the vacant layers in the structures. Since Nb^{5+} and Ta^{5+} ions are similar in size (64 pm; both cations are 6-fold coordinated) at the octahedral sites,[29] this is consistent with the more polarizable Nb^{5+} cation by neighboring oxygen anions being better able to adapt to the less symmetrical environment of the B1 site than Ta^{5+}.[30]

The effect of the Ta/Nb ratio on the morphology of $Ba_5Nb_{4-x}Ta_xO_{15}$ crystals was observed by SEM, and the results are shown in Fig. 2. As shown in Fig. 2a, large $Ba_5Nb_4O_{15}$

Table 2 Chemical compositions of $Ba_5Nb_{4-x}Ta_xO_{15}$ crystals analyzed by ICP-OES

Sample	Ba	Ta	Nb	K
$Ba_5Nb_4O_{15}$	4.974 ± 0.18	0.001 ± 0.01	4.001 ± 0.27	0.024 ± 0.02
$Ba_5TaNb_3O_{15}$	4.986 ± 0.23	1.002 ± 0.04	2.984 ± 0.09	0.028 ± 0.03
$Ba_5Ta_2Nb_2O_{15}$	4.981 ± 0.21	1.996 ± 0.06	1.997 ± 0.09	0.026 ± 0.02
$Ba_5Ta_3NbO_{15}$	4.983 ± 0.23	3.001 ± 0.10	0.985 ± 0.03	0.031 ± 0.04
$Ba_5Ta_4O_{15}$	4.980 ± 0.19	3.990 ± 0.15	0.001 ± 0.01	0.029 ± 0.03

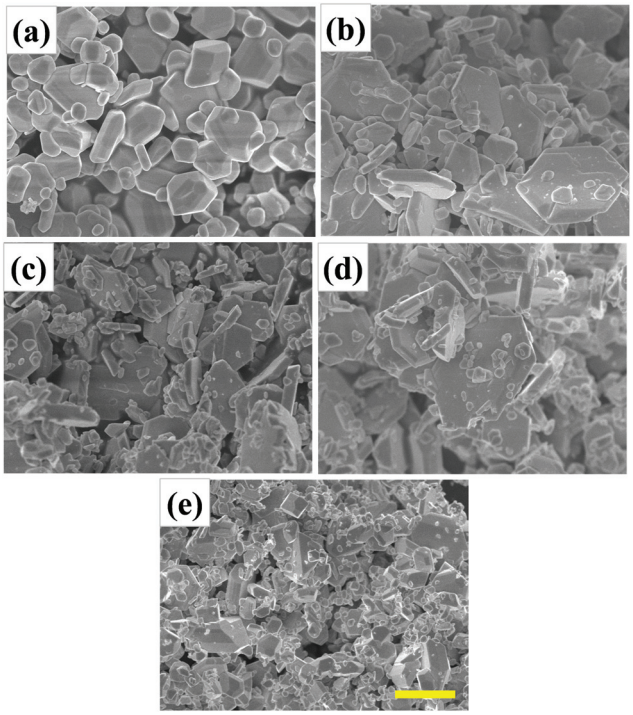

Fig. 2 SEM images of (a) $Ba_5Nb_4O_{15}$, (b) $Ba_5Nb_3TaO_{15}$, (c) $Ba_5Nb_2Ta_2O_{15}$, (d) $Ba_5NbTa_3O_{15}$, and (e) $Ba_5Ta_4O_{15}$ crystals. The scale bar is 4 μm.

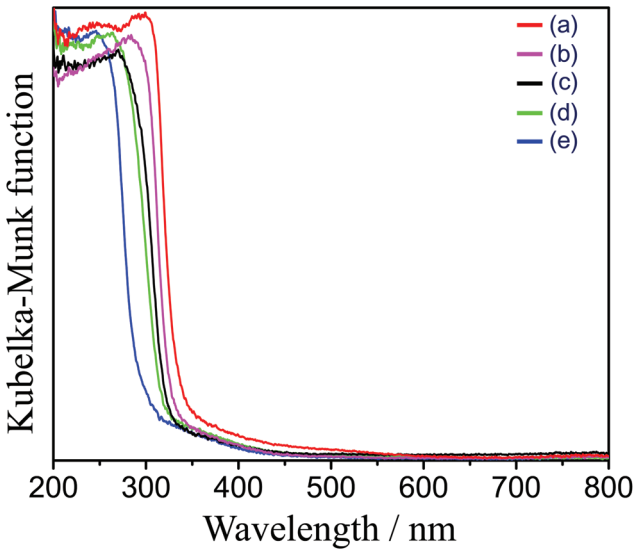

Fig. 3 UV-Vis diffuse reflectance spectra of (a) $Ba_5Nb_4O_{15}$, (b) $Ba_5Nb_3TaO_{15}$, (c) $Ba_5Nb_2Ta_2O_{15}$, (d) $Ba_5NbTa_3O_{15}$, and (e) $Ba_5Ta_4O_{15}$ crystals.

crystals have an idiomorphic shape with developed faces, whereas large $Ba_5Ta_4O_{15}$ crystals are somewhat in the form of truncated octahedra (Fig. 2e). Both samples contain large and small crystals but the difference between the sizes of large and small crystals is greater in the latter one. With the increasing Ta/Nb ratio, the $Ba_5Nb_{4-x}Ta_xO_{15}$ (x = 1–3) crystals became less faceted and gained their platelet-type hexagonal crystal habits with the thickness of <0.5 μm and lateral size of <8 μm (Fig. 2b–d) as a result of the mixed NbO_6- and TaO_6-octahedra, lowering the total interfacial energy and leading to anisotropic growth. As suggested by Madaro *et al.*,[31] the connectivity of octahedra can determine the aspect ratio of the crystals.

The ultraviolet-visible (UV-Vis) diffuse reflectance spectra of $Ba_5Nb_{4-x}Ta_xO_{15}$ crystals are plotted in Fig. 3. The $Ba_5Nb_{4-x}Ta_xO_{15}$ crystals exhibited a strong absorption in the ultraviolet region due to the band-to-band transition. With the increasing Ta/Nb ratio, the absorption edge was gradually shifted toward shorter wavelengths (from 345 to 311 nm), confirming that $Ba_5Nb_4O_{15}$ has a slightly smaller band gap (E_g = 3.59 eV) compared to $Ba_5Ta_4O_{15}$ (E_g = 3.98 eV), and $Ba_5Nb_{4-x}Ta_xO_{15}$ crystals can be applied in UV-light-driven photocatalytic processes.

The XRD patterns of the $BaNb_{1-x}Ta_xO_2N$ ($0 \le x \le 1$) samples are shown in Fig. 4. Clearly, the diffraction patterns of the samples are almost identical to that of $BaNbO_2N$, which is in good agreement with the cubic perovskite structure with the space group $Pm\bar{3}m$ (ICDD PDF 84-1749). The complete phase transition from hexagonal $Ba_5Nb_{4-x}Ta_xO_{15}$ to cubic $BaNb_{1-x}Ta_xO_2N$ was succeeded by high-temperature nitridation for an extended period without forming any impurity phases. With the increasing Ta/Nb ratio, the diffraction peaks were slightly shifted toward a higher angle, expediting the contraction of the lattice parameters due to the replacement of niobium by tantalum in the $BaNbO_2N$ lattice.[32]

As shown in Fig. 5, the $BaNb_{1-x}Ta_xO_2N$ ($0 \le x \le 1$) samples have porous structures compared to their dense precursor $Ba_5Nb_{4-x}Ta_xO_{15}$ ($0 \le x \le 4$) crystals with smooth surfaces. Although the outlines of the oxide precursor crystals were nearly maintained, the $BaNb_{1-x}Ta_xO_2N$ porous structures were formed owing to the oxide-to-oxynitride phase transition and lattice condensation process as well as lattice shrinkage because of partial replacement of O^{2-} with N^{3-} in the crystal lattice of oxide precursors during the nitridation process.[33,34] Apparently, the number of large pores in the $BaNb_{1-x}Ta_xO_2N$ crystal structures was reduced with the increasing Ta/Nb ratio. The EDS element mapping images and spectra (Fig. S1 in the ESI†) and ICP-OES results (Table 3) confirm that tantalum and niobium are homogeneously distributed, and the Ta/Nb molar ratio is close to the stoichiometric mixtures of starting materials.

The UV-Vis diffuse reflectance spectra of $BaNb_{1-x}Ta_xO_2N$ ($0 \le x \le 1$) are shown in Fig. 5. The absorption edge of $BaNbO_2N$ is found to be at approximately 720 nm and is slightly shifted toward shorter wavelengths ($\lambda \approx 690$ nm) with the increasing Ta/Nb ratio, evidencing an increment in the optical band gap. The intensity of background absorption, stemming from the existence of reduced niobium species and anion deficiency, beyond the absorption edge wavelength, is gradually declined with the increasing Ta/Nb ratio. The digital images suggest that the color of the $BaNb_{1-x}Ta_xO_2N$ powders is changed from dark brown to light brown with the increasing Ta/Nb ratio, showing the difference in light absorption due to the change in the optical band gap.

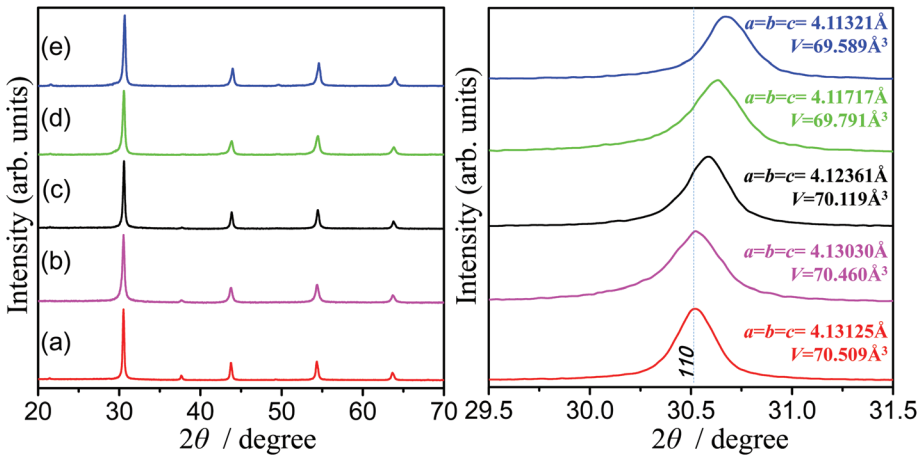

Fig. 4 XRD patterns of (a) $BaNbO_2N$, (b) $BaNb_{0.75}Ta_{0.25}O_2N$, (c) $BaNb_{0.50}Ta_{0.50}O_2N$, (d) $BaNb_{0.25}Ta_{0.75}O_2N$, and (e) $BaTaO_2N$ crystal structures synthesized by nitriding the flux-grown $Ba_5Nb_{4-x}Ta_xO_{15}$ ($0 \leq x \leq 4$) crystals at 950 °C for 20, 25, 30, 35, and 40 h under an NH_3 flow.

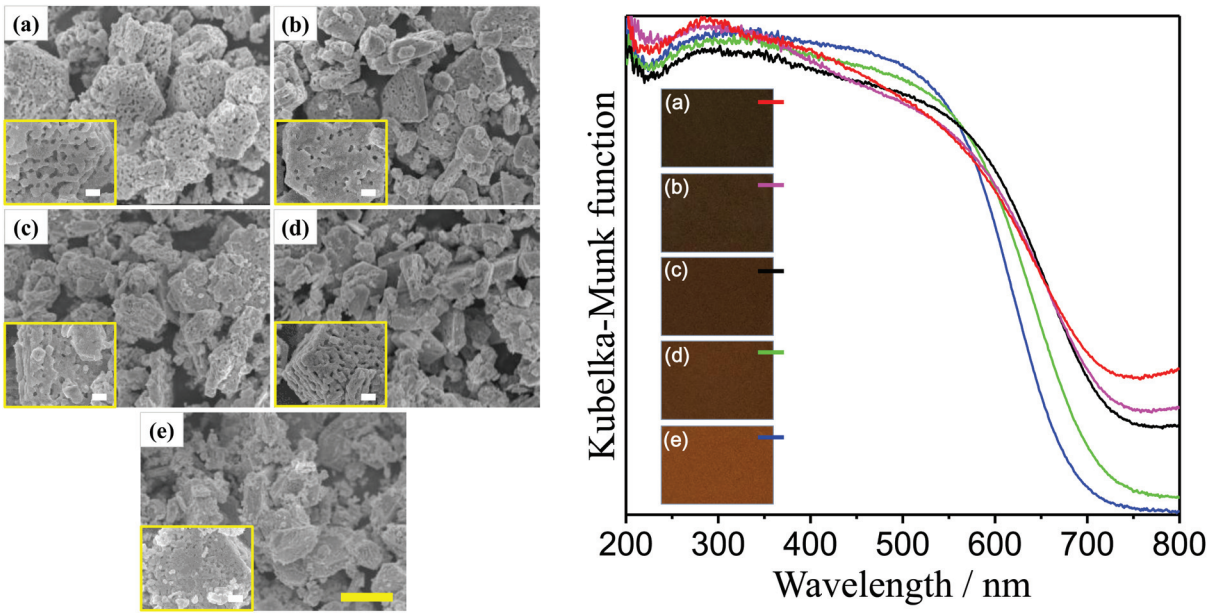

Fig. 5 SEM images (left) and UV-Vis diffuse reflectance spectra (right) of (a) $BaNbO_2N$, (b) $BaNb_{0.75}Ta_{0.25}O_2N$, (c) $BaNb_{0.50}Ta_{0.50}O_2N$, (d) $BaNb_{0.25}Ta_{0.75}O_2N$, and (e) $BaTaO_2N$ crystal structures. The scale bar is 2 μm, and the scale bar in insets is 300 nm.

Table 3 Chemical compositions, specific surface areas, and O_2 evolution rates of $BaNb_{1-x}Ta_xO_2N$ crystal structures

Sample	Ba	Ta	Nb	S_{BET} ($m^2\ g^{-1}$)	O_2 evolution rate, μmol in 2 h
$BaNbO_2N$	1.000 ± 0.11	0.001 ± 0.00	0.999 ± 0.11	15.64 ± 4.2	20.92 ± 2.2
$BaTa_{0.25}Nb_{0.75}O_2N$	0.994 ± 0.10	0.254 ± 0.03	0.752 ± 0.06	15.38 ± 4.1	30.16 ± 2.7
$BaTa_{0.50}Nb_{0.50}O_2N$	1.000 ± 0.11	0.503 ± 0.05	0.497 ± 0.04	12.52 ± 2.8	127.24 ± 9.2
$BaTa_{0.75}Nb_{0.25}O_2N$	0.997 ± 0.09	0.748 ± 0.07	0.255 ± 0.03	7.93 ± 2.1	61.63 ± 5.2
$BaTaO_2N$	0.998 ± 0.09	0.999 ± 0.10	0.003 ± 0.00	5.01 ± 1.8	38.50 ± 3.7

The XPS core-level spectra of Ba 3d, Nb 3d, Ta 4f, O 1s, and N 1s of $BaNb_{1-x}Ta_xO_2N$ ($0 \leq x \leq 1$) are shown in Fig. 6. In the Ba 3d spectra, two peaks are observed at 795.56 and 780.34 eV, representing the $3d_{3/2}$ and $3d_{5/2}$ components, respectively. The Nb $3d_{5/2}$ and Nb $3d_{3/2}$ peaks appear at 207.22 and 209.96 eV, respectively, confirming that niobium is entirely in the oxidation state of +5. The Ta $4f_{7/2}$ and Ta $4f_{5/2}$ peaks noted at 26.12 and 28.11 eV can be assigned to

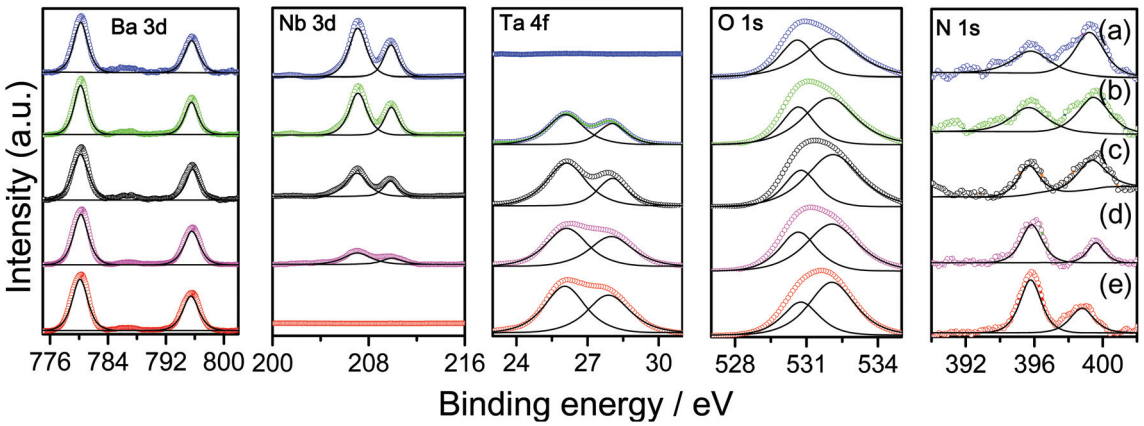

Fig. 6 High resolution XPS core-level spectra of Ba 3d, Nb 3d, Ta 4f, O 1s, and N 1s of (a) $BaNbO_2N$, (b) $BaNb_{0.75}Ta_{0.25}O_2N$, (c) $BaNb_{0.50}Ta_{0.50}O_2N$, (d) $BaNb_{0.25}Ta_{0.75}O_2N$, and (e) $BaTaO_2N$ crystal structures.

Ta^{5+}. With the increasing Ta/Nb ratio, the intensity of the Ta 4f peaks is gradually increased, while the intensity of the Nb 3d peaks becomes less pronounced and eventually disappears. The deconvoluted O 1s peaks centered at 530.84 and 532.05 eV are associated with lattice oxygen and surface adsorbed oxygen, respectively. The N 1s peaks appearing at about 395 and 399 eV are ascribed to lattice nitrogen and surface-adsorbed nitrogen species and interstitial nitrogen, respectively.[32] With the increasing Ta/Nb ratio, the N 1s peak at 395 eV became more pronounced, while a contrary event was seen in the peak at 399 eV, suggesting that more nitrogen was possibly introduced substitutionally into the lattice with a higher tantalum content. However, in order to quantify the exact concentrations of interstitial and substitutional nitrogen present in the samples and to distinguish surface-adsorbed nitrogen species with interstitial nitrogen, further studies are needed. An increase in the Ta/Nb ratio led to the introduction of more substitutional nitrogen reaching its limited amount and further displacing nitrogen into an interstitial location in $BaNb_{1-x}Ta_xO_2N$. Interestingly, a decrease in the Ta/Nb ratio displayed a contrary phenomenon. Since the top of the valence band of $BaNbO_2N$ is less positively positioned than the oxidation potential of H_2O/O_2 (1.23 V), an isolated N 2p narrow band, which consists of interstitial nitrogen and is located just above the valence band maximum (VBM) mainly composed of hybridized O 2p and N 2p states, can additionally contribute to the enhancement of photocatalytic water oxidation activity of samples with higher Ta/Nb ratios due to their enhanced light absorption and narrowed band gap.[35,36]

The reaction time courses of O_2 evolution over $BaNb_{1-x}Ta_xO_2N$ ($0 \leq x \leq 1$) loaded with CoO_x (2 wt% Co) nanoparticles under visible light are presented in Fig. 7. Compared with $BaNbO_2N$, the $BaNb_{1-x}Ta_xO_2N$ crystal structures exhibited higher O_2 evolution rates due to the increased Ta/Nb ratio, allowing the top of the valence band of $BaNbO_2N$ to be more positively positioned than the oxidation potential of H_2O/O_2 (1.23 V). The O_2 evolution rate progressed in the following order: 20.92 < 30.16 < 38.50 < 61.63 < 127.24 μmol in the first 2 h for $BaNbO_2N$, $BaNb_{0.75}Ta_{0.25}O_2N$, $BaTaO_2N$, $BaNb_{0.25}Ta_{0.75}O_2N$, and $BaNb_{0.50}Ta_{0.50}O_2N$, respectively. Surprisingly, the $BaNb_{0.50}Ta_{0.50}O_2N$ showed the highest O_2 evolution rate (127.24 μmol in the first 2 h) among the samples; however, a further increase in the Ta/Nb ratio ($BaNb_{0.25}Ta_{0.75}O_2N$ and $BaTaO_2N$) resulted in an abrupt reduction in the O_2 evolution rate. This peculiar conjuncture can be presumably related to the reduced specific surface area (Table 3) and high density of structural defects, such as grain boundaries that may act as recombination centers, originating from the prolonged high-temperature nitridation.[37]

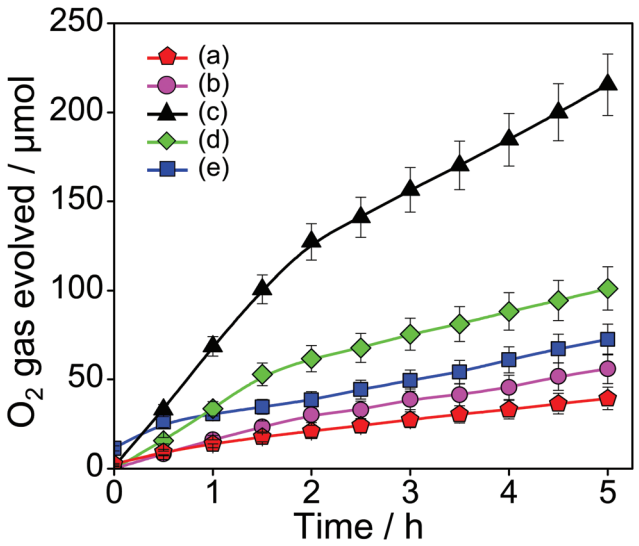

Fig. 7 Reaction time courses for the photocatalytic oxygen evolution over (a) $BaNbO_2N$, (b) $BaNb_{0.75}Ta_{0.25}O_2N$, (c) $BaNb_{0.50}Ta_{0.50}O_2N$, (d) $BaNb_{0.25}Ta_{0.75}O_2N$, and (e) $BaTaO_2N$ crystal structures under visible light irradiation. Photocatalytic reaction conditions: 100 mg photocatalyst loaded with CoO_x cocatalyst (2 wt% Co); 300 mL aqueous solution of $AgNO_3$ (10 mM); 200 mg La_2O_3 (pH buffer); light source – 300 W Xe lamp fitted with a cold mirror (CM-1) and a cutoff filter (λ > 420 nm); a side-irradiation-type reaction vessel was used in this study.

To better understand the complex carrier dynamics associated with the photocatalytic water oxidation, the $BaNb_{1-x}Ta_xO_2N$ ($0 \leq x \leq 1$) samples were further studied by transient absorption spectroscopy (TAS), and the TA spectra of $BaNb_{1-x}Ta_xO_2N$ ($0 \leq x \leq 1$) after the band-gap photoexcitation are shown in Fig. 8. Clearly, all samples showed absorption peaks at 15 000 cm^{-1} assignable to photogenerated holes. Similarly, absorption peaks located in the visible light region were also observed previously for $LaTiO_2N$,[21,22] $BaTaO_2N$,[38] and Ta_3N_5.[34] The intensity of the absorption peaks at 15 000 cm^{-1} was notably changed with the Ta content (Fig. 9a). That is, the intensity increased with increasing the Ta content up to 50 mol% but decreased at 75 and 100 mol%. The number of surviving holes is larger in the order of $BaNb_{0.5}Ta_{0.5}O_2N$ > $BaNb_{0.75}Ta_{0.25}O_2N$ > $BaNbO_2N$ > $BaNb_{0.25}Ta_{0.75}O_2N$ > $BaTaO_2N$. In the case of absorption from 14 000 to 3000 cm^{-1}, the spectral shape was drastically changed with increasing the Ta content. Namely, the negative absorption was observed for $BaNbO_2N$, whereas a very broad and positive absorption was noted for $BaTaO_2N$. As a result, the absorption intensity at 10 000 cm^{-1} was monotonically increased with increasing the Ta content (Fig. 9b), of which $BaTaO_2N$ (100 mol% Ta) exhibited the highest intensity. The broad absorption is assigned to deeply trapped electrons and/or holes at the defects, whereas the negative absorption is ascribed to some bleaching effects.[39] Absorption in the mid-IR region (<4000 cm^{-1}) is associated with free electrons and/or shallowly trapped electrons.[38] The number of surviving electrons observed at 1400 cm^{-1} was increased with increasing the Ta content up to 75 mol% and slightly decreased at 100 mol% (Fig. 9c). The above results suggest that the number of surviving holes (Fig. 9a) is strongly correlated with the photocatalytic activity for O_2 evolution (Fig. 7), *i.e.* the greater the number of surviving holes the higher activity is. It is worth to mention here that if the number of surviving holes is higher, the number of surviving electrons should also be higher.[40] However, the contradicting fact noticed here is accounted for the overlapping with the negative broad absorption at 14 000–3000 cm^{-1}. In the steady-state absorption spectra, shown in Fig. 5 and S2 in the ESI,† the broad absorption is already present at 10 000 and 1400 cm^{-1} for $BaNbO_2N$ without a pump pulse. The absorption intensity was monotonically decreased with increasing the Ta content. As reported,[41] this broad absorption assigned to electrons trapped at the defects is present for $BaNbO_2N$ but absent for $BaTaO_2N$. That is, the absorption intensity was gradually increased by filling the defects with electrons. Therefore, the negative absorption in the TA spectra of $BaNbO_2N$ is ascribed to the optical bleaching effects.[39] That is, when the trapped electrons existing before irradiation are photoexcited, the number of trapped electrons decreases. Therefore, it is concluded that the absorption intensities at 10 000 and 1400 cm^{-1} do not precisely reflect the actual number of trapped- and free electrons, respectively. This is the reason why the absorption intensity at 10 000–1000 cm^{-1} is not correlated with the photocatalytic activity results (Fig. 7) but the intensity at 15 000 cm^{-1} is well correlated with photocatalytic activity for the water oxidation of $BaNb_{1-x}Ta_xO_2N$ ($0 \leq x \leq 1$).

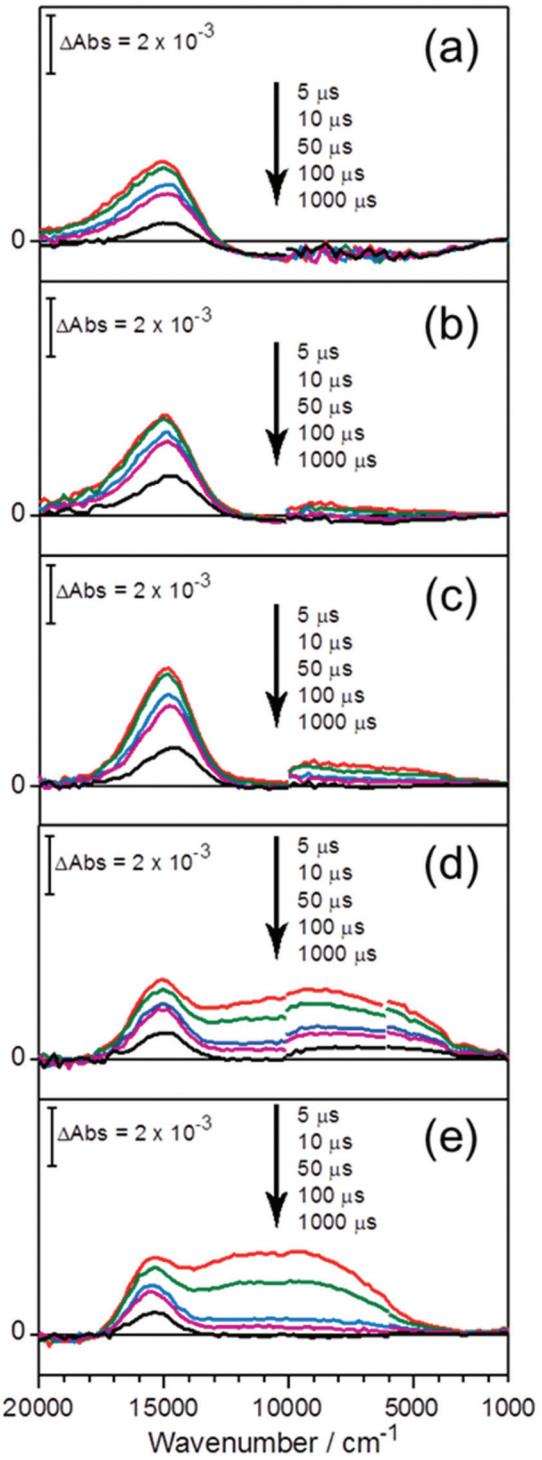

Fig. 8 Transient absorption spectra of (a) $BaNbO_2N$, (b) $BaNb_{0.75}Ta_{0.25}O_2N$, (c) $BaNb_{0.50}Ta_{0.50}O_2N$, (d) $BaNb_{0.25}Ta_{0.75}O_2N$, and (e) $BaTaO_2N$ crystal structures. All samples were excited by using 355 nm laser pulses with a pump energy of 0.5 mJ per pulse.

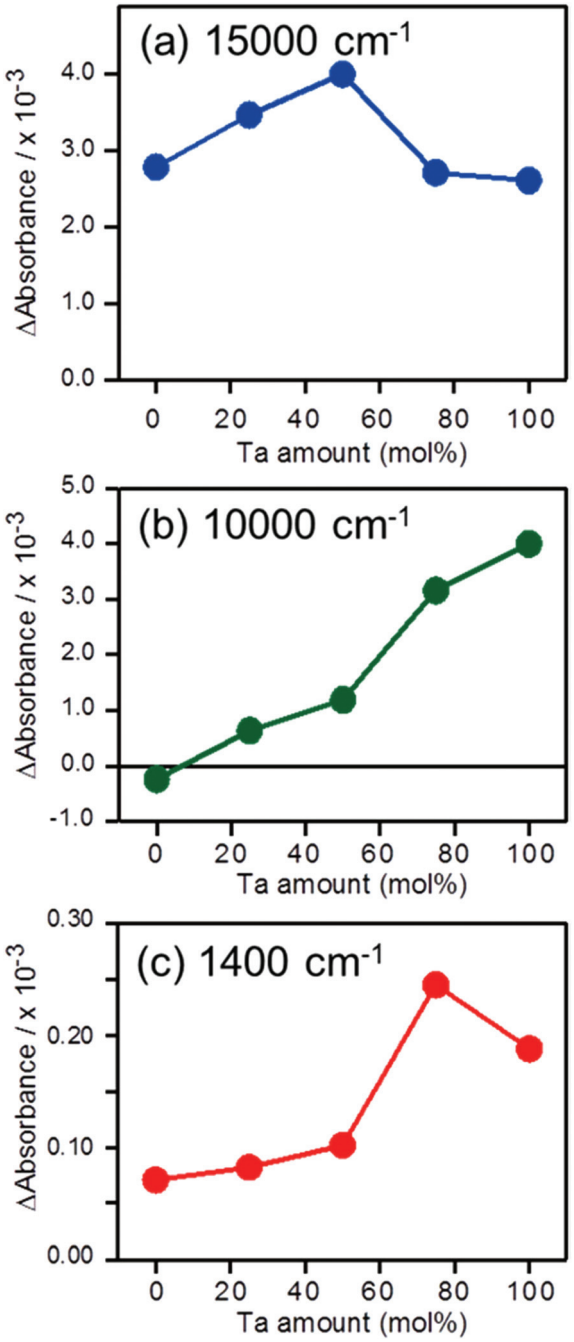

Fig. 9 Dependence of the number of surviving holes (a), trapped carriers (b), and free electrons (c) on the Ta content in $BaNb_{1-x}Ta_xO_2N$ ($0 \leq x \leq 1$) crystal structures. The absorbance intensity was obtained at 5 μs delay time and the pump energy was 0.5 mJ per pulse.

4. Conclusions

In summary, we studied the effect of the Ta/Nb ratio in the (111)-layered B-site deficient hexagonal perovskite $Ba_5Nb_{4-x}Ta_xO_{15}$ ($0 \leq x \leq 4$) crystals on visible-light-induced photocatalytic water oxidation activity of their oxynitride derivatives $BaNb_{1-x}Ta_xO_2N$ ($0 \leq x \leq 1$). The Rietveld analysis revealed that $Ba_5Nb_{4-x}Ta_xO_{15}$ crystals were well crystallized in the space group $P\bar{3}m1$ (no. 164). The highest O_2 evolution rate (127.24 μmol in the first 2 h) was achieved with the Ta content at 50 mol%, and a further decrease at 75 and 100 mol% was assumed to be the result of the reduced specific surface area and high density of structural defects, such as grain boundaries acting as recombination centers. The outcome from transient absorption spectroscopy led us to a better understanding of the effect of the Ta/Nb ratio on the behavior and energy states of the photogenerated charge carriers as well as photocatalytic water oxidation activities of $BaNb_{1-x}Ta_xO_2N$ ($0 \leq x \leq 1$) crystal structures.

Acknowledgements

This research was supported in part by the Japan Technological Research Association of Artificial Photosynthetic Chemical Process (ARPChem). The authors thank Mr. Kenta Kawashima of Shinshu University, Japan, for his kind assistance in evaluating the photocatalytic water oxidation activity.

Notes and references

1 P. J. Boddy, *J. Electrochem. Soc.*, 1968, **115**, 199–203.
2 A. Fujishima and K. Honda, *Nature*, 1972, **238**, 37–38.
3 O. Khaselev and J. A. Turner, *Science*, 1998, **280**, 425–427.
4 F. E. Osterloh and B. A. Parkinson, *MRS Bull.*, 2011, **36**, 17–22.
5 K. Maeda and K. Domen, *J. Phys. Chem. C*, 2007, **111**, 7851–7861.
6 K. Domen, J. Yoshimura, T. Sekine, A. Tanaka and T. Onishi, *Catal. Lett.*, 1990, **4**, 339–343.
7 K. Maeda and T. E. Mallouk, *J. Mater. Chem.*, 2009, **19**, 4813–4818.
8 H. Otsuka, K. Kim, A. Kouzu, I. Takimoto, H. Fujimori, Y. Sakata, H. Imamura, T. Matsumoto and K. Toda, *Chem. Lett.*, 2005, **34**, 822–823.
9 Y. Miseki, H. Kato and A. Kudo, *Chem. Lett.*, 2006, **35**, 1052–1053.
10 K. Yoshioka, V. Petrykin, M. Kakihana, H. Kato and A. Kudo, *J. Catal.*, 2005, **232**, 102–107.
11 Y. Miseki, H. Kato and A. Kudo, *Energy Environ. Sci.*, 2009, **2**, 306–314.
12 T.-G. Xu, C. Zhang, X. Shao, K. Wu and Y.-F. Zhu, *Adv. Funct. Mater.*, 2006, **16**, 1599–1607.
13 S. Park, H. J. Song, C. W. Lee, S. W. Hwang and I. S. Cho, *ACS Appl. Mater. Interfaces*, 2015, **7**, 21860–21867.
14 J. Soldat, R. Marschall and M. Wark, *Chem. Sci.*, 2014, **5**, 3746–3752.
15 R. Marschall, J. Soldat and M. Wark, *Photochem. Photobiol. Sci.*, 2013, **12**, 671–677.
16 J. Soldat, G. W. Busser, M. Muhler and M. Wark, *ChemCatChem*, 2016, **8**, 153–156.
17 N. C. Hildebrandt, J. Soldat and R. Marschall, *Small*, 2015, **11**, 2051–2057.

18 A. Mukherji, C. Sun, S. C. Smith, G. Q. Lu and L. Wang, *J. Phys. Chem. C*, 2011, **115**, 15674–15678.
19 J. Rodriguez-Carvajal, Fullprof: A Program for Rietveld Refinement and Pattern Matching Analysis, in *Collected Abstract of Powder Diffraction Meeting*, Toulouse, France, 1990.
20 L. W. Finger, D. E. Cox and A. P. Kephcoat, *J. Appl. Crystallogr.*, 1994, **27**, 892–900.
21 A. Yamakata, M. Kawaguchi, N. Nishimura, T. Minegishi, J. Kubota and K. Domen, *J. Phys. Chem. C*, 2014, **118**, 23897–23906.
22 K. Kawashima, M. Hojamberdiev, H. Wagata, K. Yubuta, J. J. M. Vequizo, A. Yamakata, S. Oishi, K. Domen and K. Teshima, *J. Phys. Chem. C*, 2015, **119**, 15896–15904.
23 A. Yamakata, H. Yeilin, M. Kawaguchi, T. Hisatomi, J. Kubota, Y. Sakata and K. Domen, *J. Photochem. Photobiol., A*, 2015, **313**, 168–175.
24 A. Yamakata, J. J. M. Vequizo and M. Kawaguchi, *J. Phys. Chem. C*, 2015, **119**, 1880–1885.
25 A. Yamakata, J. J. M. Vequizo and H. Matsunaga, *J. Phys. Chem. C*, 2015, **119**, 24538–24545.
26 T. A. Vanderah, T. R. Collins, W. Wong-Ng, R. S. Roth and L. Farber, *J. Alloys Compd.*, 2002, **346**, 116–128.
27 J. Shannon and L. Katz, *Acta Crystallogr., Sect. B: Struct. Crystallogr. Cryst. Chem.*, 1970, **26**, 102–105.
28 S. Pagola, G. Polla, G. Leyva, M. T. Casais, J. A. Alonso, I. Rasines and R. E. Carbonio, *European Powder Diffraction: Epdic Iv, Pts 1 and 2*, 1996, **228**, 819–824.
29 R. D. Shannon, *Acta Crystallogr., Sect. A: Cryst. Phys., Diffr., Theor. Gen. Cryst.*, 1976, **32**, 751–767.
30 H. Weitzel, *Z. Kristallogr.*, 1976, **144**, 238–258.
31 F. Madaro, R. Sæterli, J. R. Tolchard, M.-A. Einarsrud, R. Holmestad and T. Grande, *CrystEngComm*, 2011, **13**, 1304–1313.
32 M. Hojamberdiev, E. Zahedi, E. Nurlaela, K. Kawashima, K. Yubuta, M. Nakayama, H. Wagata, T. Minegishi, K. Domen and K. Teshima, *J. Mater. Chem. A*, 2016, DOI: 10.1039/C6TA03786K.
33 K. Kawashima, M. Hojamberdiev, H. Wagata, K. Yubuta, S. Oishi and K. Teshima, *Cryst. Growth Des.*, 2015, **15**, 333–339.
34 M. Hojamberdiev, H. Wagata, K. Yubuta, K. Kawashima, J. J. M. Vequizo, A. Yamakata, S. Oishi and K. Teshima, *Appl. Catal., B*, 2016, **182**, 626–635.
35 F. Peng, L. Cai, H. Yu, H. Wang and J. Yang, *J. Solid State Chem.*, 2008, **181**, 130–136.
36 K. Kawashima, M. Hojamberdiev, H. Wagata, E. Zahedi, K. Yubuta, S. Oishi, K. Domen and K. Teshima, Two-Step Synthesis and Visible-Light-Driven Photocatalytic Water Oxidation Activity of AW(O,N)$_3$ (A = Sr, La, Pr, Nd and Eu) Perovskites, *CrystEngComm*, submitted.
37 S. C. Warren, K. Voïtchovsky, H. Dotan, C. M. Leroy, M. Cornuz, F. Stellacci, C. Hébert, A. Rothschild and M. Grätzel, *Nat. Mater.*, 2013, **12**, 842–849.
38 M. Hojamberdiev, K. Yubuta, J. J. M. Vequizo, A. Yamakata, S. Oishi, K. Domen and K. Teshima, *Cryst. Growth Des.*, 2015, **15**, 4663–4671.
39 S. Sorenson, E. Driscoll, S. Haghighat and J. M. Dawlaty, *J. Phys. Chem. C*, 2014, **118**, 23621–23626.
40 K. Kawashima, M. Hojamberdiev, H. Wagata, M. Nakayama, K. Yubuta, S. Oishi, K. Domen and K. Teshima, *Catal. Sci. Technol.*, 2016, **6**, 5389–5396.
41 Y.-L. Kim, P. M. Woodward, K. Z. Baba-Kishi and C. W. Tai, *Chem. Mater.*, 2004, **16**, 1267–1276.